
Evaluating Foundation Models’ 3D Understanding Through Multi-View Correspondence Analysis

Valentina Lilova*

University of Amsterdam
Amsterdam, 1098 XH

valentina.lilova@student.uva.nl

Toyesh Chakravorty*

University of Amsterdam
Amsterdam, 1098 XH

toyesh.chakravorty@student.uva.nl

Julian I. Bibo*

University of Amsterdam
Amsterdam, 1098 XH

julian.bibo@student.uva.nl

Emma Boccaletti*

University of Amsterdam
Amsterdam, 1098 XH

emma.boccaletti@student.uva.nl

Brandon Li*

University of Amsterdam
Amsterdam, 1098 XH

brandon.li@student.uva.nl

Lívia Baxová*

University of Amsterdam
Amsterdam, 1098 XH

livia.baxova@student.uva.nl

Cees G. M. Snoek

University of Amsterdam
Amsterdam, 1098 XH

c.g.m.snoek@uva.nl

Mohammadreza Salehi

University of Amsterdam
Amsterdam, 1098 XH

s.salehidenavi@uva.nl

Editors: Marco Fumero, Clementine Domine, Zorah Lähner, Irene Cannistraci, Bo Zhao, Alex Williams

Abstract

Benchmarking 3D spatial understanding of foundation models is essential for real-world applications such as robotics and autonomous driving. Existing evaluations often rely on downstream fine-tuning with linear heads or task-specific decoders, making it difficult to isolate the intrinsic 3D reasoning ability of pre-trained encoders. In this work, we introduce a novel benchmark for in-context 3D scene understanding that requires no fine-tuning and directly probes the quality of dense visual features. Building on the Hummingbird framework, which evaluates in-context 2D scene understanding, we extend the setup to the 3D Multi-View ImageNet (MVImgNet) dataset. Given a set of images depicting objects at specific camera angles (keys), we benchmark the performance of segmenting novel views (queries) and report the scores in 4 categories of easy, medium, hard, and extreme based on the key-query view contrast. We benchmark 7 state-of-the-art foundation models and show that DINO-based encoders remain competitive across large viewpoint shifts. Our code is publicly available at <https://github.com/ToyeshC/open-hummingbird-3d-eval>.

*Equal contribution.

1 Introduction

In recent years, we have seen the rise of foundation models [2, 28, 15, 32]. These large-scale pre-trained models support many tasks, including visual understanding, which enables direct comparison of their encoders. Despite their impressive capabilities, state-of-the-art Vision Transformers (ViTs) can suffer catastrophic failures when objects are viewed from unusual angles, as demonstrated by recent angle-sensitivity studies [20]. However, most vision benchmarks emphasize single-view tasks or dense synthesis [14, 17, 21, 22, 35], leaving segmentation robustness under camera rotations comparatively underexplored.

To address viewpoint variability, recent work has explored in-context learning (ICL) as a means to adapt models to unseen views without retraining. ICL is the ability of a model to perform new tasks by conditioning on a prompt [31]. An example is Hummingbird [1], a memory-augmented ViT for ICL. Its encoder extracts dense image features and projects them into key-value pairs stored in a dynamic memory. At query time, cross-attention over the keys assigns soft nearest-neighbor (NN) weights to aggregate values and predict novel views in-context. This modular design permits the use of any encoder.

In this work, we evaluate general-purpose ViT encoders [18, 3, 16, 27, 29, 8, 13] for in-context object segmentation under unseen camera viewpoints. We extend the Hummingbird evaluation framework with the Multi-View ImageNet (MVIImgNet) dataset [34], grouping object views into angular bins. By constructing memory banks consisting of images from specific viewpoints and evaluating segmentation performance on held-out angles, we assess how well different encoders generalize across viewpoint shifts. Our main contribution combines three elements: (1) pixel-level segmentation, (2) extreme viewpoint changes, and (3) dynamic memory for ICL. Most existing work studies 3D understanding, but there is little evaluation of how consistent the features from frozen 2D foundation models remain when the camera moves to new viewpoints and only a few in-context examples are available.

2 Related work

Recent developments in view generation have significantly improved the understanding of 3D scene structure in computer vision, setting new benchmarks along the way. For example, Neural Radiance Fields (NeRFs) [14] achieve state-of-the-art novel view synthesis by optimizing a continuous volumetric function from sparse input images. While NeRFs addresses generation, other studies investigate recognition in 3D understanding. Ruan et al. [20] demonstrate that modern recognition models (ResNets [6], ViTs [4], Swin [12], and Masked Autoencoders (MAEs) [7]) remain sensitive to viewpoint shifts in 3D scenes. With adversarial training, they improve invariance to 3D viewpoint changes beyond standard rotation-based augmentations. In parallel, Shifman and Weiss [26] show that state-of-the-art encoders such as CLIP and DINOv2 change predictions under a single-pixel shift in up to 40% of cases, despite extensive augmentation during training. Although their analysis centers on 2D translation invariance, the findings highlight that robustness to geometric changes, whether in 2D or 3D, remains limited in current vision encoders.

At a higher level, previous benchmarks in 3D computer vision were generally divided into two groups. The first group includes those working on traditional 3D recognition tasks, such as item detection (e.g., KITTI, Waymo [11, 9]) or scene segmentation (e.g., SAI3D, ScanNet [33]), which typically test explicit 3D architectures or employ classification/bounding box tasks. The second focuses on innovative view synthesis approaches, such as NeRF [14], which prioritize dense creation rather than robust detection or segmentation under angular deviation. Beyond these 3D-focused benchmarks, general ICL benchmarks such as the Hummingbird framework [1] or post-training approaches [22, 21, 17, 35] assess feature transferability only in a 2D setting, and therefore fail to evaluate models under non-linear, wide-angle 3D viewpoint shifts.

Beyond model architectures, multi-view datasets such as MVIImgNet and PASCAL3D+ [30] offer rich multi-view annotations that support the evaluation of cross-view generalization in object recognition. The rise of self-supervised Transformers has also opened new possibilities for downstream tasks such as segmentation. In particular, DINOv2 [3] produces robust embeddings that transfer effectively to prediction tasks, despite training without labels. More recently, Siméoni et al. [27] introduced DINOv3, which significantly scales the DINOv2 framework. A critical technical contribution of

DINOv3 is the introduction of Gram Anchoring, a mechanism designed to prevent the degradation of dense feature maps during long-duration self-supervised training. By regularizing patch-level similarity structures against a teacher model, this model maintains high-quality spatial features that are crucial for dense prediction tasks.

Nevertheless, a gap remains across these benchmarks and models. Most prior work emphasizes detection, classification, or view-angle estimation, but not the measurement of 3D contextual understanding through multi-view segmentation. To address this, our benchmark primarily evaluates general-purpose foundation encoders. To our knowledge, no existing benchmark systematically evaluates a model’s ability to generalize segmentation across viewpoint shifts using dynamic memory. Our proposed evaluation method aims to address this gap in existing research.

3 Methodology

We evaluate the view generalization ability of frozen ViT models in semantic segmentation using a non-parametric, retrieval-based framework. Our approach builds on the Hummingbird framework [1], which applies ICL to vision tasks and supports the evaluation of spatial perception and semantic understanding. However, Hummingbird does not analyze performance variations across viewpoints changes. To address this, we introduce a viewpoint binning protocol and a multi-view dataset subset for cross-view robustness analysis. License information for the models, framework, and dataset can be found in Appendix A.

3.1 Models

We evaluate 7 pre-trained ViTs: CLIP [18], SigLIP2 [29], DINO [3], DINOv2 [16], DINOv3 [27], C-RADIOv2 [19, 8], and TIPS [13]. Most models use a ViT-B/16 backbone, except DINOv2 and TIPS, which have a ViT-B/14 backbone.

3.2 Inference pipeline

We follow the Hummingbird [1] inference pipeline, where patch-level features from a frozen ViT are stored in a memory bank with one-hot semantic labels. During inference, query features are matched to the memory using FAISS² with cosine similarity and $k = 30$ nearest neighbors. The memory size is passed as an input parameter. Hummingbird’s cross-attention decoder aggregates the retrieved labels to produce segmentation predictions.

3.3 Dataset

Our study is based on MVIImgNet, a large-scale dataset with over 6.5 million frames across 238 object categories [34]. Each frame includes a segmentation mask, camera extrinsics, and a reconstructed 3D point cloud. This dataset is chosen for three reasons: (1) it contains various annotations across wide viewpoint ranges, enabling view generalization analysis; (2) it includes camera extrinsics that allow precise angular binning; and (3) it has scale and diversity, capturing a broad range of object appearances and spatial configurations.

3.3.1 Viewpoint binning

To study viewpoint robustness, we discretize relative camera angles into 7 bins spanning 0° – 90° , in steps of 15° . To aid in this task, we use COLMAP [23–25]: a Structure-from-Motion (SfM) and Multi-View Stereo (MVS) pipeline that estimates camera poses and 3D scene geometry from a set of images. Using COLMAP extrinsics, we compute the relative rotation R_{rel} between each frame and the first frame of the object instance. For each instance, we select 1 representative frame per bin by choosing the frame with the smallest angular error relative to the bin center. Images and masks are stored per bin for downstream use. The angular deviation θ is computed as

²Facebook AI Similarity Search (FAISS) is an open-source library designed for efficient similarity search and clustering of dense vectors, optimized for high-dimensional feature retrieval [10].

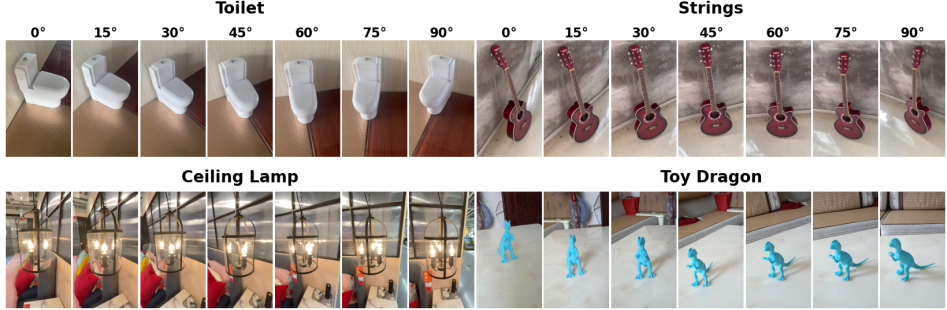


Figure 1: **Multi-view instances**. Each MVImgNet category contains instances spanning all discretized viewpoint bins between 0° and 90° . The figure shows example visualizations of 4 instances from the 15 selected classes.

$$\theta = \arccos \left(\frac{\text{trace}(R_{rel}) - 1}{2} \right). \quad (1)$$

3.3.2 Subset construction

We curated a subset of MVImgNet, with the goal of selecting categories (classes) with sufficient angular coverage and manageable size for repeated memory-based evaluation. The two criteria used for selecting a category are: (1) the total zipped folder size must be 1–6 GB to ensure feasible data loading and storage; and (2) at least one object instance must span all 7 angular bins with a maximum variance of 6° . Categories that did not meet these criteria were excluded. For example, category 23 (*laptop*) was excluded, as it did not have an instance that reached an angle of 90° . This yielded 15 segmentation classes, excluding the background.³

For each category instance, we parsed the COLMAP camera pose data to extract camera extrinsics and compute relative angles. For each valid instance, we selected the closest frame to each angular bin center and organized the resulting RGB images and masks in a structured directory grouped by category and angle. Additionally, we computed angular selection errors per bin (see Table 6). Examples of different views of several class instances from the resulting dataset are shown in Figure 1.

3.4 Model input

To ensure a fair comparison, we use the largest native input size across all models. This is 504×504 for models that use a patch size of 14 and 512×512 for the ones using a patch size of 16. When evaluating models at resolutions higher than those used during pre-training, we resize the pre-trained absolute positional embeddings to match the new patch grid using bicubic interpolation. All evaluations are performed with a batch size of 4. The full configuration details are provided in Appendix C.

3.5 Metrics and multi-view evaluation

The segmentation quality is measured by mean Intersection over Union (mIoU) across all semantic classes. Each predicted segmentation mask consists of the background class and one of the 15 object classes. We report 3 metrics for each evaluation setting: the per-class Intersection over Union (IoU), also known as the Jaccard index, mIoU over all 16 classes, and standard deviation. Results are presented per model, reference bin, and validation bin to analyze viewpoint robustness. Although all models perform well on the background class (see Figure 5), we include it in the mIoU computation for completeness.

³The 15 categories are ordered as follows: stove, sofa, microwave, bed, toy cat, toy cow, toy dragon, coat rack, guitar stand, ceiling lamp, toilet, sink, strings, broccoli, and durian. More details can be found in Appendix B.

Table 1: **Difficulties and bin splits.** Difficulty levels are defined by the choice of reference bins (stored in the memory bank) and validation bins (unseen views for testing generalization). An increasing difficulty corresponds to fewer reference bins and larger unseen angular gaps, which makes interpolation and extrapolation progressively harder.

Difficulty	Reference bins	Validation bins
Easy	$0^\circ, 30^\circ, 60^\circ, 90^\circ$	$15^\circ, 45^\circ, 75^\circ$
Medium	$0^\circ, 45^\circ, 90^\circ$	$15^\circ, 30^\circ, 60^\circ, 75^\circ$
Hard	$0^\circ, 90^\circ$	$15^\circ, 30^\circ, 45^\circ, 60^\circ, 75^\circ$
Extreme	0°	$15^\circ, 30^\circ, 45^\circ, 60^\circ, 75^\circ, 90^\circ$

Table 2: **mIoU scores across difficulty levels.** For each model, we report the average mIoU and standard deviation over the 4 difficulty levels. The memory size used is 1,024k. DINOv3 achieves the best performance across all difficulties, followed by DINOv2 and DINO, of which the latter outperformed DINOv2 in the Easy and Medium setups (where multiple reference views are available). DINOv2 significantly outperformed DINO under the Extreme case with only a single reference bin.

Model	Easy	Medium	Hard	Extreme
CLIP ViT-B/16	0.755 ± 0.130	0.748 ± 0.134	0.734 ± 0.140	0.701 ± 0.149
DINO ViT-B/16	0.782 ± 0.132	0.774 ± 0.137	0.748 ± 0.153	0.686 ± 0.171
DINOv2 ViT-B/14	0.763 ± 0.136	0.758 ± 0.139	0.748 ± 0.143	0.728 ± 0.154
DINOv3 ViT-B/16	0.809 ± 0.130	0.803 ± 0.133	0.790 ± 0.144	0.773 ± 0.158
C-RADIOv2 ViT-B/16-CPE	0.653 ± 0.129	0.636 ± 0.132	0.592 ± 0.141	0.506 ± 0.150
SigLIP2 B/16-512	0.564 ± 0.150	0.551 ± 0.153	0.530 ± 0.157	0.481 ± 0.152
TIPS ViT-B/14-HR	0.667 ± 0.137	0.647 ± 0.146	0.588 ± 0.162	0.462 ± 0.169

4 Experimental results

To validate our setup, we first reproduced the Hummingbird evaluation on PASCAL VOC [5] using the official open-source implementation.⁴ The results, shown in Table 8 of Appendix E, match the methodology and configuration of the original paper [1]. This confirms that our pipeline is consistent with the benchmark and provides a reliable basis for the experiments that follow.

With the setup validated, we proceed to evaluate viewpoint generalization and robustness across 3 experiments: (A) cross-viewpoint generalization, (B) breaking point analysis, and (C) memory size robustness.

4.1 Experiment A: cross-viewpoint generalization

We compare the models in terms of their ability to generalize across viewpoints. The goal is to assess how different pre-training strategies affect performance when only limited reference views are available in the memory. Specifically, we evaluate how well the models generalize to unseen viewpoints when trained on selected angular bins from the MVIImgNet dataset. The reference and validation splits vary across 4 difficulty levels, which are summarized in Table 1. Each model is evaluated using the mIoU across all 16 classes (background and 15 object categories) and all validation images. This setup enables a controlled comparison of each model’s ability to interpolate between observed viewpoints and extrapolate to unseen ones.

4.1.1 Results

As shown in Table 2, DINOv3 outperformed all models across all difficulties. DINO had the second-best performance for the Easy and Medium difficulty levels. Quantitative results illustrating these trends are shown in Figure 2, with per-class results in Appendix F.1. Across all classes, DINOv3 and DINOv2 maintain stronger segmentation performance as difficulty increases, with DINO remaining competitive under most settings. CLIP performs close to the DINO models and surpasses DINO under the Extreme setting, while C-RADIOv2, TIPS, and SigLIP2 perform noticeably worse, particularly when reference views are limited.

⁴The evaluation repository can be found at <https://github.com/vpariza/open-hummingbird-eval>.

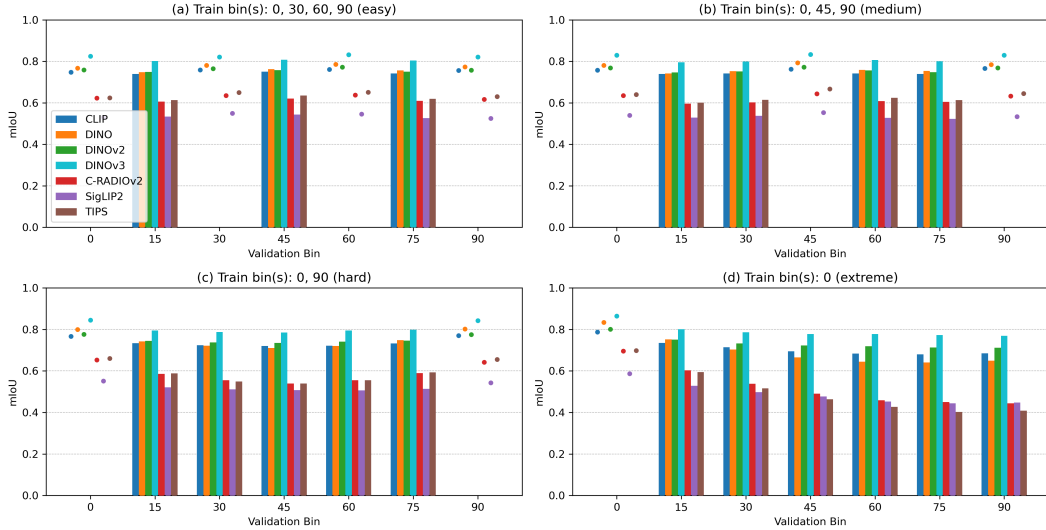


Figure 2: **Segmentation performance across viewpoint bins.** Each subplot (a)–(d) corresponds to a different difficulty level. Bars show mIoU scores on unseen validation bins, while dots show performance on the reference bins stored in the memory bank. The figure illustrates how segmentation accuracy declines as the validation angles move farther from the reference viewpoints. DINOv3, DINOv2, DINO, and CLIP maintain higher, more stable performance as angular distance increases, whereas other models degrade more quickly. Overall, the trend highlights how self-supervised pre-training leads to smoother cross-view generalization.

4.1.2 Discussion

Although none of the models were explicitly trained for viewpoint understanding, the results show clear differences in their ability to generalize across views. As seen in the previous section, DINOv3 performs best, followed by DINOv2 and DINO. This suggests that the features of the DINO models, compared to other models, are more stable under viewpoint changes and better support shape-related cues. This consistency may arise from their self-supervised training objective, which explicitly encourages feature alignment across multiple augmentations of the same image and more stable relationships between local and global representations. DINOv3 further benefits from large-scale pre-training and the Gram Anchoring mechanism [27], which might contribute to more stable local features and stronger geometric consistency under viewpoint changes.

While DINO performed better under the easier difficulties, where multiple views of the object were available, DINOv2 obtained a higher mIoU under the Extreme difficulty with only 1 reference bin. One possible interpretation is that DINO’s simpler self-distillation loss favors interpolation across views, whereas DINOv2’s larger-scale self-supervised pre-training better supports generalization to more extreme viewpoints. CLIP generally ranked third, reflecting some ability to encode visual-semantic regularities despite being trained for image-text alignment rather than geometric consistency. By comparison, SigLIP2, TIPS, and C-RADIOv2 performed substantially worse, suggesting that objectives centered on semantic matching or mixed supervision may weaken part-level consistency needed for viewpoint-robust segmentation.

4.2 Experiment B: breaking point analysis

In this experiment, we analyze whether the models experience a sudden failure in viewpoint generalization, and if so, at what angle. The goal is to identify the angular range within which performance remains stable under the Extreme difficulty. In particular, we perform a breaking point analysis under the Extreme setting from experiment A, where only a single reference bin (0°) is available in the memory and models are evaluated across the remaining bins. We define the breaking point as the

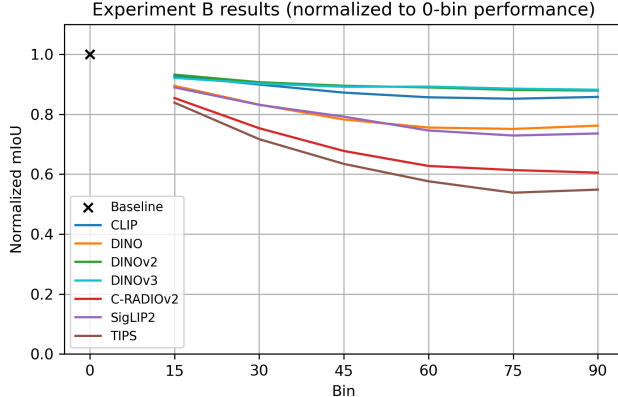


Figure 3: **Normalized mIoU under viewpoint shifts.** Each curve shows the normalized mIoU of a model relative to its performance in the 0° reference bin. The horizontal axis corresponds to increasing viewpoint angles (validation bins). All models exhibit a monotonic decrease with diminishing slope, indicating that the steepest performance degradation occurs at the initial viewpoint shifts, followed by progressively flatter declines at larger angles. DINOv3, DINOv2, and CLIP degrade smoothly, followed by DINO and SigLIP2, whereas TIPS and C-RADIOv2 display sharper early drops, suggesting weaker robustness to small viewpoint changes.

earliest validation bin where a model’s normalized mIoU score \tilde{m}_i drops significantly compared to the previous bin (\tilde{m}_{i-1}). Specifically, we compute the performance drop Δ_i per bin i as

$$\Delta_i = \tilde{m}_i - \tilde{m}_{i-1}, \quad (2)$$

$$\tilde{m}_i = \frac{m_i}{m_{0^\circ}}, \quad (3)$$

where the normalization by the 0° bin (Equation 3) ensures that performance drops reflect viewpoint sensitivity rather than overall model scale or performance.

A breaking point is recorded at bin i if $\Delta_i \leq -0.1$, indicating a relative drop of 10% or more. This analysis highlights each model’s resistance to viewpoint shifts and identifies the angular range within which performance remains stable. We also report the normalized mIoU degradation curves as the viewpoint angle increases.

4.2.1 Results

As shown in Figure 3, all models exhibit a monotonic decrease in normalized mIoU as the validation viewpoint angle increases. The drop is steepest at small viewpoint changes and gradually flattens at larger angles, indicating that most performance degradation occurs at the initial viewpoint shifts.

TIPS is the only model that reaches a breaking point, occurring at the 30° bin (see Table 3), with a normalized mIoU drop of -0.1148 . C-RADIOv2 shows a relatively sharp early decline but remains below the breaking-point threshold. DINOv3, DINOv2, and CLIP exhibit the smoothest degradation, followed by DINO and SigLIP2.

4.2.2 Discussion

The breaking point analysis highlights differences in robustness across models and shows how their pre-training objectives affect stability under viewpoint shifts. DINOv2 and DINOv3 are the most stable, maintaining gradual degradation without sudden drops. CLIP shows a similar trend, with slightly weaker overall performance. The normalized performances of DINO and SigLIP2 also decrease steadily, with a slight increase at the 90° bin. Interestingly, CLIP and SigLIP2 preserve some resilience despite being trained for image-text alignment rather than spatial structure. Although C-RADIOv2 does not reach a breaking point, it comes very close to one, which we could

Table 3: **Breaking points.** For each model, we report the breaking point validation bin where the normalized mIoU drop exceeds 10% ($\Delta_i \leq -0.1$) relative to the previous bin. “None” indicates gradual degradation. Only TIPS reaches a breaking point. C-RADIOv2 is close to having a breaking point, but it doesn’t pass the threshold as per our definition. DINO, DINOv2, CLIP, and SigLIP2 maintain smoother decline curves. The biggest drops for all models occur between 15° and 30° as seen in Figure 3.

Model	Breaking point bin	Biggest drop
CLIP ViT-B/16	None	-0.0267
DINO ViT-B/16	None	-0.0559
DINOv2 ViT-B/14	None	-0.0273
DINOv3 ViT-B/16	None	-0.0214
C-RADIOv2 ViT-B/16-CPE	None	-0.0969
SigLIP2 B/16-512	None	-0.0550
TIPS ViT-B/14-HR	30	-0.1148

attribute to its mixed supervision weakening the reliability of part-level representations. In contrast, TIPS exhibits a clear breakdown, suggesting that its learned features are less robust when faced with unseen viewpoints. This instability may stem from its focus on semantic alignment rather than spatial consistency. Relative to the baseline that includes validation bins in the memory, the observed drops can be attributed to missing reference views rather than to instability in the evaluation pipeline. Overall, the results suggest that self-supervised encoders such as the DINO-based models produce more geometry-aware features under strong viewpoint shifts, while multimodal or distilled approaches may be more brittle. DINOv2 and DINOv3’s stability make them the most reliable choice for applications that must handle abrupt perspective changes.

4.3 Experiment C: memory size robustness

In this final experiment, we analyze how memory bank size affects viewpoint generalization, comparing the performance gains across difficulty levels against the added computational cost. We follow the Hummingbird paper [1] and vary the number of entries in the memory bank. Three memory sizes are evaluated: 320k, 640k, and 1,024k. For each size, we report the segmentation accuracy.

4.3.1 Results

The results in Table 4 show that increasing the memory bank generally improves mIoU, with the largest gains observed under the Easy difficulty. Doubling the memory from 320k to 640k increases performance by approximately 0.030 mIoU on Easy, while a further increase to 1,024k yields a smaller improvement of 0.017 (see Table 9 in Appendix F.3).

DINOv3 achieves the highest absolute performance across all memory sizes, followed by DINO and DINOv2. Weaker models such as C-RADIOv2, SigLIP2, and TIPS benefit more from additional memory, improving by more than 0.048 mIoU when increasing the memory from 320k to 1,024k, with most of the gain coming from the first doubling of memory.

Increasing the memory bank introduces additional practical considerations, as documented in Appendix F.3.

4.3.2 Discussion

These results confirm that larger memory banks improve generalization, but the benefits vary across models. Less robust encoders such as C-RADIOv2, SigLIP2, and TIPS gain the most from additional memory, while DINOv3, DINO, and DINOv2 already perform strongly even with smaller banks. The diminishing gains beyond 640k and the higher computational cost suggest that the intermediate configuration offers the best trade-off. This shows that memory scaling can compensate for weaker representations, but stable self-supervised features remain more effective overall.

Table 4: **Comparison of memory-bank size on segmentation performance.** Mean mIoU scores and standard deviations are shown for 3 memory sizes ((a) 320k, (b) 640k, (c) 1,024k) and 4 difficulty levels. Bold values mark the best score per difficulty-memory configuration. Increasing memory generally improves performance, especially for weaker encoders such as SigLIP2. The DINO models remain the top performers across all settings, but have minimal gains past 640k.

Model	Easy	Medium	Hard	Extreme
(a) Memory: 320k				
CLIP ViT-B/16	0.729 ± 0.138	0.725 ± 0.141	0.710 ± 0.149	0.681 ± 0.156
DINO ViT-B/16	0.741 ± 0.147	0.736 ± 0.150	0.712 ± 0.163	0.656 ± 0.178
DINOv2 ViT-B/14	0.738 ± 0.145	0.736 ± 0.146	0.726 ± 0.152	0.709 ± 0.158
DINOv3 ViT-B/16	0.793 ± 0.139	0.788 ± 0.141	0.780 ± 0.149	0.768 ± 0.157
C-RADIOv2 ViT-B/16-CPE	0.588 ± 0.136	0.579 ± 0.139	0.539 ± 0.146	0.467 ± 0.149
SigLIP2 B/16-512	0.506 ± 0.154	0.501 ± 0.156	0.483 ± 0.157	0.443 ± 0.149
TIPS ViT-B/14-HR	0.600 ± 0.161	0.590 ± 0.166	0.539 ± 0.178	0.437 ± 0.175
(b) Memory: 640k				
CLIP ViT-B/16	0.745 ± 0.132	0.740 ± 0.136	0.727 ± 0.141	0.694 ± 0.150
DINO ViT-B/16	0.768 ± 0.137	0.761 ± 0.141	0.736 ± 0.156	0.676 ± 0.173
DINOv2 ViT-B/14	0.754 ± 0.138	0.750 ± 0.142	0.740 ± 0.147	0.721 ± 0.155
DINOv3 ViT-B/16	0.803 ± 0.133	0.798 ± 0.136	0.787 ± 0.145	0.771 ± 0.157
C-RADIOv2 ViT-B/16-CPE	0.629 ± 0.132	0.615 ± 0.135	0.572 ± 0.142	0.491 ± 0.150
SigLIP2 B/16-512	0.541 ± 0.152	0.531 ± 0.154	0.511 ± 0.157	0.466 ± 0.149
TIPS ViT-B/14-HR	0.644 ± 0.144	0.628 ± 0.153	0.571 ± 0.167	0.453 ± 0.170
(c) Memory: 1,024k				
CLIP ViT-B/16	0.755 ± 0.130	0.748 ± 0.134	0.734 ± 0.140	0.701 ± 0.149
DINO ViT-B/16	0.782 ± 0.132	0.774 ± 0.137	0.748 ± 0.153	0.686 ± 0.171
DINOv2 ViT-B/14	0.763 ± 0.136	0.758 ± 0.139	0.748 ± 0.143	0.728 ± 0.154
DINOv3 ViT-B/16	0.809 ± 0.130	0.803 ± 0.133	0.790 ± 0.144	0.773 ± 0.158
C-RADIOv2 ViT-B/16-CPE	0.653 ± 0.129	0.636 ± 0.132	0.592 ± 0.141	0.506 ± 0.150
SigLIP2 B/16-512	0.564 ± 0.150	0.551 ± 0.153	0.530 ± 0.157	0.481 ± 0.152
TIPS ViT-B/14-HR	0.667 ± 0.137	0.647 ± 0.146	0.588 ± 0.162	0.462 ± 0.169

5 Qualitative analysis of segmentations

In addition to quantitative evaluations, we conducted a qualitative inspection of predicted segmentation masks to better understand model behavior under the large-angle changes of the Extreme difficulty. The illustrations mentioned in this section can be found in Appendix G.

5.1 Localized shape recovery

As illustrated in Figure 28, models generally segment the global shape of an object even when the viewpoint differs substantially from any reference view. Although predictions (center) are not perfectly pixel-aligned with the ground truth (left), the overall contour and structure are typically preserved. Minor over-extensions at the ends of the object (e.g., protruding elements like a tail) are common, reflecting the limits of fine-grained spatial recall under large angular deviations.

5.2 Prediction versus ground truth overlays

Overlays of the predicted mask (center) versus the ground truth (left) on the input image, such as those in Figure 29, reveal systematic patterns: models tend to underestimate boundaries in regions with strong self-occlusion or low illumination, while occasionally oversegmenting areas with visually similar textures or shadows. Despite these deviations, the predictions largely align with the main visual cues of the target object, suggesting strong local feature retrieval even from distant viewpoints.

5.3 Prediction versus ground truth

Color-coded difference maps (e.g., Figure 29 (right), or Figure 30) show that most misalignments occur near object borders or in thin, high-curvature regions (e.g., legs, tails). This indicates that memory retrieval may struggle with fine-grained spatial resolution under Extreme difficulty views. As illustrated in Figures 7 and 21–26 for the *bed* class, some categories may have imprecise or inconsistent ground truth masks which contribute to measured errors, sometimes penalizing predictions that are visually more plausible. Such cases highlight that annotation quality can limit the reliability of quantitative evaluation, since metrics are tied to imperfect labels rather than perceptual correctness.

5.4 Failures

Failure cases, such as the *toy dragon* shown in Figure 30, typically arise when the model retrieves visually similar but geometrically inconsistent patches. This may lead to boundary inflation. Such failures may explain the sharp performance drops observed in certain models (e.g., TIPS) at larger angular deviations, where cross-view consistency becomes more challenging.

6 Conclusion

We studied the ability of frozen ViT encoders to generalize across unseen camera viewpoints in an in-context segmentation setting, using the Hummingbird architecture and MVIImgNet dataset. Our benchmark covered three aspects: controlled evaluation under view shifts, robustness through breaking point analysis, and the effect of memory bank size. Our findings show that self-supervised encoders, particularly DINO, DINOv2, and DINOv3, achieve higher performance under viewpoint changes than multimodal and mixed-supervision approaches. Increasing the memory bank size benefits weaker models and offers diminishing returns for stronger encoders.

Taken together, these results highlight the strengths and limitations of current ViTs for multi-view perception. While self-supervised training objectives are associated with improved robustness, none of the models are immune to viewpoint-induced degradation. Addressing this gap will likely require objectives or architectures that more explicitly account for 3D or viewpoint consistency. Future work could include extending this evaluation to multi-object or multi-class scenes, wider angular ranges, and compound rotations, providing a broader testbed for building truly viewpoint-robust representations.

References

- [1] Ivana Balažević, David Steiner, Nikhil Parthasarathy, Relja Arandjelović, and Olivier J. Hénaff. Towards in-context scene understanding. In *Advances in Neural Information Processing Systems*, volume 36, pages 63758–63778. Curran Associates, Inc., 2023. URL https://proceedings.neurips.cc/paper_files/paper/2023/file/c94a632545000531f0b47000e9caa5b6-Paper-Conference.pdf.
- [2] Rishi Bommasani, Drew A. Hudson, Ehsan Adeli, Russ Altman, Simran Arora, Sydney von Arx, Michael S. Bernstein, Jeannette Bohg, Antoine Bosselut, Emma Brunskill, Erik Brynjolfsson, Shyamal Buch, Dallas Card, Rodrigo Castellon, Niladri Chatterji, Annie Chen, Kathleen Creel, Jared Quincy Davis, Dora Demszky, Chris Donahue, Moussa Doumbouya, Esin Durmus, Stefano Ermon, John Etchemendy, Kawin Ethayarajh, Li Fei-Fei, Chelsea Finn, Trevor Gale, Lauren Gillespie, Karan Goel, Noah Goodman, Shelby Grossman, Neel Guha, Tatsunori Hashimoto, Peter Henderson, John Hewitt, Daniel E. Ho, Jenny Hong, Kyle Hsu, Jing Huang, Thomas Icard, Saahil Jain, Dan Jurafsky, Pratyusha Kalluri, Siddharth Karamcheti, Geoff Keeling, Fereshte Khani, Omar Khattab, Pang Wei Koh, Mark Krass, Ranjay Krishna, Rohith Kuditipudi, Ananya Kumar, Faisal Ladhak, Mina Lee, Tony Lee, Jure Leskovec, Isabelle Levent, Xiang Lisa Li, Xuechen Li, Tengyu Ma, Ali Malik, Christopher D. Manning, Suvir Mirchandani, Eric Mitchell, Zanele Munyikwa, Suraj Nair, Avanika Narayan, Deepak Narayanan, Ben Newman, Allen Nie, Juan Carlos Niebles, Hamed Nilforoshan, Julian Nyarko, Giray Ogut, Laurel Orr, Isabel Papadimitriou, Joon Sung Park, Chris Piech, Eva Portelance, Christopher Potts, Aditi Raghunathan, Rob Reich, Hongyu Ren, Frieda Rong, Yusuf Roohani, Camilo Ruiz, Jack Ryan, Christopher Ré, Dorsa Sadigh, Shiori Sagawa, Keshav Santhanam, Andy Shih, Krishnan

Srinivasan, Alex Tamkin, Rohan Taori, Armin W. Thomas, Florian Tramèr, Rose E. Wang, William Wang, Bohan Wu, Jiajun Wu, Yuhuai Wu, Sang Michael Xie, Michihiro Yasunaga, Jiaxuan You, Matei Zaharia, Michael Zhang, Tianyi Zhang, Xikun Zhang, Yuhui Zhang, Lucia Zheng, Kaitlyn Zhou, and Percy Liang. On the opportunities and risks of foundation models, 2022. URL <https://arxiv.org/abs/2108.07258>.

- [3] Mathilde Caron, Hugo Touvron, Ishan Misra, Hervé Jegou, Julien Mairal, Piotr Bojanowski, and Armand Joulin. Emerging properties in self-supervised vision transformers. In *2021 IEEE/CVF International Conference on Computer Vision (ICCV)*, pages 9630–9640, 2021. doi: 10.1109/ICCV48922.2021.00951.
- [4] Alexey Dosovitskiy, Lucas Beyer, Alexander Kolesnikov, Dirk Weissenborn, Xiaohua Zhai, Thomas Unterthiner, Mostafa Dehghani, Matthias Minderer, Georg Heigold, Sylvain Gelly, Jakoba Uszkoreit, and Neil Houlsby. An Image is Worth 16x16 Words: Transformers for Image Recognition at Scale. In *International Conference on Learning Representations*, 2020.
- [5] Mark Everingham, Luc Van Gool, Christopher K. I. Williams, John Winn, and Andrew Zisserman. The Pascal Visual Object Classes (VOC) Challenge. *Int. J. Comput. Vision*, 88(2):303–338, June 2010. ISSN 1573-1405. doi: 10.1007/s11263-009-0275-4.
- [6] Kaiming He, Xiangyu Zhang, Shaoqing Ren, and Jian Sun. Deep residual learning for image recognition. In *2016 IEEE Conference on Computer Vision and Pattern Recognition (CVPR)*, pages 770–778, 2016. doi: 10.1109/CVPR.2016.90.
- [7] Kaiming He, Xinlei Chen, Saining Xie, Yanghao Li, Piotr Dollár, and Ross Girshick. Masked autoencoders are scalable vision learners. In *2022 IEEE/CVF Conference on Computer Vision and Pattern Recognition (CVPR)*, pages 15979–15988, 2022. doi: 10.1109/CVPR52688.2022.01553.
- [8] Greg Heinrich, Mike Ranzinger, Hongxu Danny Yin, Yao Lu, Jan Kautz, Andrew Tao, Bryan Catanzaro, and Pavlo Molchanov. Radiov2.5: Improved baselines for agglomerative vision foundation models. In *2025 IEEE/CVF Conference on Computer Vision and Pattern Recognition (CVPR)*, pages 22487–22497, 2025. doi: 10.1109/CVPR52734.2025.02094.
- [9] Sunwook Hwang. *Improvement of Object Detection in Autonomous Driving using Communication Systems*. Ph.d. dissertation, Seoul National University, Seoul, aug 2023. URL <https://hdl.handle.net/10371/196434>. Supervised by Se-Woong Park.
- [10] Jeff Johnson, Matthijs Douze, and Hervé Jégou. Billion-scale similarity search with GPUs. *IEEE Transactions on Big Data*, 7(3):535–547, 2019.
- [11] Kana Kim, Vijay Kakani, and Hakil Kim. Automatic pruning and quality assurance of object detection datasets for autonomous driving. *Electronics*, 14(9), 2025. ISSN 2079-9292. doi: 10.3390/electronics14091882. URL <https://www.mdpi.com/2079-9292/14/9/1882>.
- [12] Ze Liu, Yutong Lin, Yue Cao, Han Hu, Yixuan Wei, Zheng Zhang, Stephen Lin, and Baining Guo. Swin transformer: Hierarchical vision transformer using shifted windows. In *Proceedings of the IEEE/CVF International Conference on Computer Vision (ICCV)*, pages 10012–10022, October 2021.
- [13] Kevins-Kokitsi Maninis, Kaifeng Chen, Soham Ghosh, Arjun Karpur, Koert Chen, Ye Xia, Bingyi Cao, Daniel Salz, Guangxing Han, Jan Dlabal, Dan Gnanapragasam, Mojtaba Seyedhosseini, Howard Zhou, and André Araujo. TIPS: Text-Image Pretraining with Spatial Awareness. In *ICLR*, 2025.
- [14] Ben Mildenhall, Pratul P. Srinivasan, Matthew Tancik, Jonathan T. Barron, Ravi Ramamoorthi, and Ren Ng. Nerf: representing scenes as neural radiance fields for view synthesis. *Commun. ACM*, 65(1):99–106, December 2021. ISSN 0001-0782. doi: 10.1145/3503250. URL <https://doi.org/10.1145/3503250>.
- [15] OpenAI, Josh Achiam, Steven Adler, Sandhini Agarwal, Lama Ahmad, Ilge Akkaya, Florencia Leoni Aleman, Diogo Almeida, Janko Altenschmidt, Sam Altman, Shyamal Anadkat, Red Avila, Igor Babuschkin, Suchir Balaji, Valerie Balcom, Paul Baltescu, Haiming Bao,

Mohammad Bavarian, Jeff Belgum, Irwan Bello, Jake Berdine, Gabriel Bernadett-Shapiro, Christopher Berner, Lenny Bogdonoff, Oleg Boiko, Madelaine Boyd, Anna-Luisa Brakman, Greg Brockman, Tim Brooks, Miles Brundage, Kevin Button, Trevor Cai, Rosie Campbell, Andrew Cann, Brittany Carey, Chelsea Carlson, Rory Carmichael, Brooke Chan, Che Chang, Fotis Chantzis, Derek Chen, Sully Chen, Ruby Chen, Jason Chen, Mark Chen, Ben Chess, Chester Cho, Casey Chu, Hyung Won Chung, Dave Cummings, Jeremiah Currier, Yunxing Dai, Cory Decareaux, Thomas Degry, Noah Deutsch, Damien Deville, Arka Dhar, David Dohan, Steve Dowling, Sheila Dunning, Adrien Ecoffet, Atty Eleti, Tyna Eloundou, David Farhi, Liam Fedus, Niko Felix, Simón Posada Fishman, Juston Forte, Isabella Fulford, Leo Gao, Elie Georges, Christian Gibson, Vik Goel, Tarun Gogineni, Gabriel Goh, Rapha Gontijo-Lopes, Jonathan Gordon, Morgan Grafstein, Scott Gray, Ryan Greene, Joshua Gross, Shixiang Shane Gu, Yufei Guo, Chris Hallacy, Jesse Han, Jeff Harris, Yuchen He, Mike Heaton, Johannes Heidecke, Chris Hesse, Alan Hickey, Wade Hickey, Peter Hoeschele, Brandon Houghton, Kenny Hsu, Shengli Hu, Xin Hu, Joost Huizinga, Shantanu Jain, Shawn Jain, Joanne Jang, Angela Jiang, Roger Jiang, Haozhun Jin, Denny Jin, Shino Jomoto, Billie Jonn, Heewoo Jun, Tomer Kaftan, Łukasz Kaiser, Ali Kamali, Ingmar Kanitscheider, Nitish Shirish Keskar, Tabarak Khan, Logan Kilpatrick, Jong Wook Kim, Christina Kim, Yongjik Kim, Jan Hendrik Kirchner, Jamie Kiro, Matt Knight, Daniel Kokotajlo, Łukasz Kondraciuk, Andrew Kondrich, Aris Konstantinidis, Kyle Kosić, Gretchen Krueger, Vishal Kuo, Michael Lampe, Ikai Lan, Teddy Lee, Jan Leike, Jade Leung, Daniel Levy, Chak Ming Li, Rachel Lim, Molly Lin, Stephanie Lin, Mateusz Litwin, Theresa Lopez, Ryan Lowe, Patricia Lue, Anna Makanju, Kim Malfacini, Sam Manning, Todor Markov, Yaniv Markovski, Bianca Martin, Katie Mayer, Andrew Mayne, Bob McGrew, Scott Mayer McKinney, Christine McLeavey, Paul McMillan, Jake McNeil, David Medina, Aalok Mehta, Jacob Menick, Luke Metz, Andrey Mishchenko, Pamela Mishkin, Vinnie Monaco, Evan Morikawa, Daniel Mossing, Tong Mu, Mira Murati, Oleg Murk, David Mély, Ashvin Nair, Reiichiro Nakano, Rajeev Nayak, Arvind Neelakantan, Richard Ngo, Hyeyoung Noh, Long Ouyang, Cullen O’Keefe, Jakub Pachocki, Alex Paino, Joe Palermo, Ashley Pantuliano, Giambattista Parascandolo, Joel Parish, Emy Parparita, Alex Passos, Mikhail Pavlov, Andrew Peng, Adam Perelman, Filipe de Avila Belbute Peres, Michael Petrov, Henrique Ponde de Oliveira Pinto, Michael, Pokorny, Michelle Pokrass, Vitchyr H. Pong, Tolly Powell, Alethea Power, Boris Power, Elizabeth Proehl, Raul Puri, Alec Radford, Jack Rae, Aditya Ramesh, Cameron Raymond, Francis Real, Kendra Rimbach, Carl Ross, Bob Rotsted, Henri Roussez, Nick Ryder, Mario Saltarelli, Ted Sanders, Shibani Santurkar, Girish Sastry, Heather Schmidt, David Schnurr, John Schulman, Daniel Selsam, Kyla Sheppard, Toki Sherbakov, Jessica Shieh, Sarah Shoker, Pranav Shyam, Szymon Sidor, Eric Sigler, Maddie Simens, Jordan Sitkin, Katarina Slama, Ian Sohl, Benjamin Sokolowsky, Yang Song, Natalie Staudacher, Felipe Petroski Such, Natalie Summers, Ilya Sutskever, Jie Tang, Nikolas Tezak, Madeleine B. Thompson, Phil Tillet, Amin Tootoonchian, Elizabeth Tseng, Preston Tuggle, Nick Turley, Jerry Tworek, Juan Felipe Cerón Uribe, Andrea Vallone, Arun Vijayvergiya, Chelsea Voss, Carroll Wainwright, Justin Jay Wang, Alvin Wang, Ben Wang, Jonathan Ward, Jason Wei, CJ Weinmann, Akila Welihinda, Peter Welinder, Jiayi Weng, Lilian Weng, Matt Wiethoff, Dave Willner, Clemens Winter, Samuel Wolrich, Hannah Wong, Lauren Workman, Sherwin Wu, Jeff Wu, Michael Wu, Kai Xiao, Tao Xu, Sarah Yoo, Kevin Yu, Qiming Yuan, Wojciech Zaremba, Rowan Zellers, Chong Zhang, Marvin Zhang, Shengjia Zhao, Tianhao Zheng, Juntang Zhuang, William Zhuk, and Barret Zoph. Gpt-4 technical report, 2024. URL <https://arxiv.org/abs/2303.08774>.

- [16] Maxime Oquab, Timothée Darct, Théo Moutakanni, Huy Vo, Marc Szafraniec, Vasil Khalidov, Pierre Fernandez, Daniel Haziza, Francisco Massa, Alaaeldin El-Nouby, Mahmoud Assran, Nicolas Ballas, Wojciech Galuba, Russell Howes, Po-Yao Huang, Shang-Wen Li, Ishan Misra, Michael Rabbat, Vasu Sharma, Gabriel Synnaeve, Hu Xu, Hervé Jegou, Julien Mairal, Patrick Labatut, Armand Joulin, and Piotr Bojanowski. Dinov2: Learning robust visual features without supervision, 2024. URL <https://arxiv.org/abs/2304.07193>.
- [17] Valentinos Pariza, Mohammadreza Salehi, Gertjan Burghouts, Francesco Locatello, and Yuki M Asano. Near, far: Patch-ordering enhances vision foundation models’ scene understanding. *arXiv preprint arXiv:2408.11054*, 2024.
- [18] Alec Radford, Jong Wook Kim, Chris Hallacy, Aditya Ramesh, Gabriel Goh, Sandhini Agarwal, Girish Sastry, Amanda Askell, Pamela Mishkin, Jack Clark, Gretchen Krueger, and Ilya Sutskever. Learning transferable visual models from natural language supervision. In

Proceedings of the 38th International Conference on Machine Learning, volume 139 of *Proceedings of Machine Learning Research*, pages 8748–8763. PMLR, 18–24 Jul 2021. URL <https://proceedings.mlr.press/v139/radford21a.html>.

- [19] Mike Ranzinger, Greg Heinrich, Jan Kautz, and Pavlo Molchanov. Am-radio: Agglomerative vision foundation model reduce all domains into one. In *Proceedings of the IEEE/CVF Conference on Computer Vision and Pattern Recognition (CVPR)*, pages 12490–12500, June 2024.
- [20] Shouwei Ruan, Yinpeng Dong, Hang Su, Jianteng Peng, Ning Chen, and Xingxing Wei. Towards viewpoint-invariant visual recognition via adversarial training. In *Proceedings of the IEEE/CVF International Conference on Computer Vision (ICCV)*, pages 4709–4719, October 2023.
- [21] Mohammadreza Salehi, Efstratios Gavves, Cees GM Snoek, and Yuki M Asano. Time does tell: Self-supervised time-tuning of dense image representations. In *Proceedings of the IEEE/CVF International Conference on Computer Vision*, pages 16536–16547, 2023.
- [22] Mohammadreza Salehi, Shashanka Venkataramanan, Ioana Simion, Efstratios Gavves, Cees GM Snoek, and Yuki M Asano. Mosic: Optimal-transport motion trajectory for dense self-supervised learning. *arXiv preprint arXiv:2506.08694*, 2025.
- [23] Johannes Lutz Schönberger and Jan-Michael Frahm. Structure-from-motion revisited. In *Conference on Computer Vision and Pattern Recognition (CVPR)*, 2016.
- [24] Johannes Lutz Schönberger, True Price, Torsten Sattler, Jan-Michael Frahm, and Marc Pollefeys. A vote-and-verify strategy for fast spatial verification in image retrieval. In *Asian Conference on Computer Vision (ACCV)*, 2016.
- [25] Johannes Lutz Schönberger, Enliang Zheng, Marc Pollefeys, and Jan-Michael Frahm. Pixelwise view selection for unstructured multi-view stereo. In *European Conference on Computer Vision (ECCV)*, 2016.
- [26] Ofir Shifman and Yair Weiss. Lost in translation: modern neural networks still struggle with small realistic image transformations. In *European Conference on Computer Vision*, pages 231–247. Springer, 2024.
- [27] Oriane Siméoni, Huy V. Vo, Maximilian Seitzer, Federico Baldassarre, Maxime Oquab, Cijo Jose, Vasil Khalidov, Marc Szafraniec, Seungeun Yi, Michaël Ramamonjisoa, Francisco Massa, Daniel Haziza, Luca Wehrstedt, Jianyuan Wang, Timothée Darcet, Théo Moutakanni, Leonel Sentana, Claire Roberts, Andrea Vedaldi, Jamie Tolan, John Brandt, Camille Couprie, Julien Mairal, Hervé Jégou, Patrick Labatut, and Piotr Bojanowski. DINOv3, 2025. URL <https://arxiv.org/abs/2508.10104>.
- [28] Hugo Touvron, Thibaut Lavril, Gautier Izacard, Xavier Martinet, Marie-Anne Lachaux, Timothée Lacroix, Baptiste Rozière, Naman Goyal, Eric Hambro, Faisal Azhar, Aurelien Rodriguez, Armand Joulin, Edouard Grave, and Guillaume Lample. Llama: Open and efficient foundation language models, 2023. URL <https://arxiv.org/abs/2302.13971>.
- [29] Michael Tschannen, Alexey Gritsenko, Xiao Wang, Muhammad Ferjad Naeem, Ibrahim Alabdulmohsin, Nikhil Parthasarathy, Talfan Evans, Lucas Beyer, Ye Xia, Basil Mustafa, Olivier Hénaff, Jeremiah Harmsen, Andreas Steiner, and Xiaohua Zhai. Siglip 2: Multilingual vision-language encoders with improved semantic understanding, localization, and dense features, 2025. URL <https://arxiv.org/abs/2502.14786>.
- [30] Yu Xiang, Roozbeh Mottaghi, and Silvio Savarese. Beyond pascal: A benchmark for 3d object detection in the wild. In *IEEE Winter Conference on Applications of Computer Vision*, pages 75–82, 2014. doi: 10.1109/WACV.2014.6836101.
- [31] Sang Michael Xie, Aditi Raghunathan, Percy Liang, and Tengyu Ma. An explanation of in-context learning as implicit bayesian inference, 2022. URL <https://arxiv.org/abs/2111.02080>.

- [32] An Yang, Anfeng Li, Baosong Yang, Beichen Zhang, Binyuan Hui, Bo Zheng, Bowen Yu, Chang Gao, Chengen Huang, Chenxu Lv, Chujie Zheng, Dayiheng Liu, Fan Zhou, Fei Huang, Feng Hu, Hao Ge, Haoran Wei, Huan Lin, Jialong Tang, Jian Yang, Jianhong Tu, Jianwei Zhang, Jianxin Yang, Jiaxi Yang, Jing Zhou, Jingren Zhou, Junyang Lin, Kai Dang, Keqin Bao, Kexin Yang, Le Yu, Lianghao Deng, Mei Li, Mingfeng Xue, Mingze Li, Pei Zhang, Peng Wang, Qin Zhu, Rui Men, Ruize Gao, Shixuan Liu, Shuang Luo, Tianhao Li, Tianyi Tang, Wenbiao Yin, Xingzhang Ren, Xinyu Wang, Xinyu Zhang, Xuancheng Ren, Yang Fan, Yang Su, Yichang Zhang, Yinger Zhang, Yu Wan, Yuqiong Liu, Zekun Wang, Zeyu Cui, Zhenru Zhang, Zhipeng Zhou, and Zihan Qiu. Qwen3 technical report, 2025. URL <https://arxiv.org/abs/2505.09388>.
- [33] Yingda Yin, Yuzheng Liu, Yang Xiao, Daniel Cohen-Or, Jingwei Huang, and Baoquan Chen. Sai3d: Segment any instance in 3d scenes. In *Proceedings of the IEEE/CVF Conference on Computer Vision and Pattern Recognition (CVPR)*, pages 3292–3302, June 2024.
- [34] Xianggang Yu, Mutian Xu, Yidan Zhang, Haolin Liu, Chongjie Ye, Yushuang Wu, Zizheng Yan, Chenming Zhu, Zhangyang Xiong, Tianyou Liang, Guanying Chen, Shuguang Cui, and Xiaoguang Han. Mvimgnet: A large-scale dataset of multi-view images. In *Proceedings of the IEEE/CVF Conference on Computer Vision and Pattern Recognition (CVPR)*, pages 9150–9161, June 2023.
- [35] Adrian Ziegler and Yuki M Asano. Self-supervised learning of object parts for semantic segmentation. In *Proceedings of the IEEE/CVF conference on computer vision and pattern recognition*, pages 14502–14511, 2022.

A Licenses for assets

All datasets and models used in this work are released under open licenses. We list them in Table 5 below.

Table 5: **Licenses for datasets and models.** All assets are used in compliance with their respective licenses.

Asset	License
MVImgNet	CC BY-NC 4.0 (code), dataset Terms of Use
Hummingbird	MIT License
CLIP	MIT
DINO	Apache 2.0
DINOv2	Apache 2.0
DINOv3	DINOv3 License
SigLIP2	Apache 2.0
C-RADIOv2	NVIDIA Open Model License
TIPS	Apache 2.0 (code), CC BY 4.0 (docs)

B The MVImgNet dataset

The statistics for the reorganized subset of MVImgNet [34] we used are shown in Table 6. The selected subset includes 15 object classes, each represented across 7 standardized angle bins: 0° , 15° , 30° , 45° , 60° , 75° , and 90° . Figure 4 shows an instance of each angle for each object class.

Table 6: **Angle selection accuracy per class.** Mean and standard deviation of angular error (in degrees) for each object class after selecting views closest to the predefined angle bins.

Class number	Category	Std. error	Mean error	Images per bin
7	Stove	1.28	0.01	197
8	Sofa	1.15	-0.04	91
19	Microwave	1.44	-0.04	120
46	Bed	1.17	-0.00	23
57	Toy cat	1.96	-0.01	783
60	Toy cow	1.96	-0.02	735
70	Toy dragon	1.62	0.01	627
99	Coat rack	1.41	-0.02	97
100	Guitar stand	1.53	0.04	218
113	Ceiling lamp	1.64	-0.03	154
125	Toilet	1.31	0.02	58
126	Sink	1.20	-0.12	30
152	Strings	1.25	0.03	192
166	Broccoli	2.04	-0.03	210
196	Durian	1.65	0.03	758

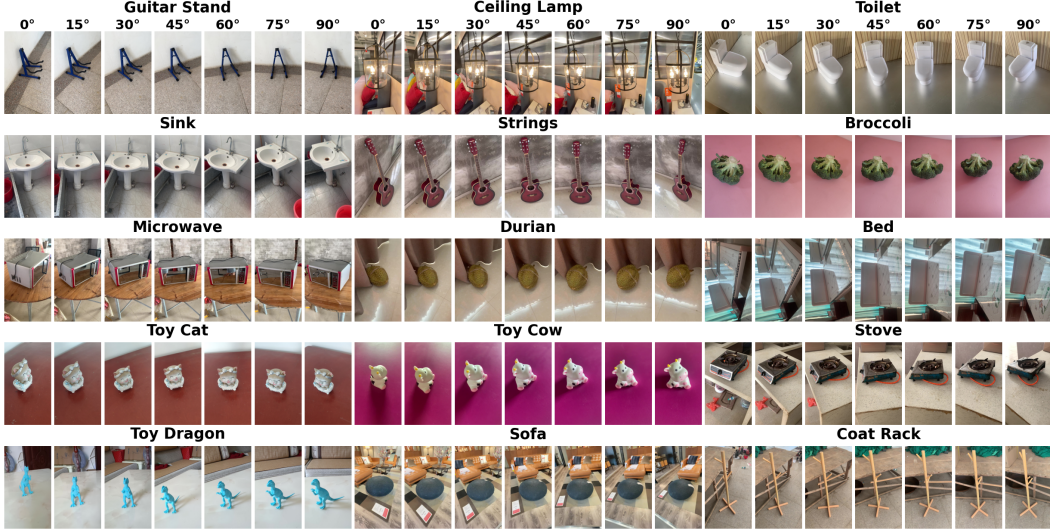


Figure 4: **Multi-view categories.** A representative instance is shown for each of the 15 selected MVImgNet classes across all viewpoint bins (0° – 90°). Based on the category taxonomy of MVImgNet [34], we have examples from both the *food* and *artifacts* parent classes, which encompass the following child classes: *fruits and vegetables*, *toy dolls*, and a series of *instruments: furniture, kitchen ware, home appliances, and entertainment*.

C Model specifics

The following table details the ViT-based encoders used in our experiments, including their patch configurations and feature dimensionality.

Table 7: **Vision Transformer configurations.** We show the architectural and input settings of the models evaluated in our experiments. Input, patch, and batch sizes are indicated with Input sz., Patch sz., and Batch sz., respectively.

Model	Architecture	Input sz.	Patch sz.	# patches	Feat. dim.	Batch sz.
DINO	ViT-B/16	512	16	1024	768	4
DINOv2	ViT-B/14	504	14	1296	768	4
DINOv3	ViT-B/16	512	16	1024	768	4
OpenAI CLIP	ViT-B/16	512	16	1024	768	4
C-RADIOv2	ViT-B/16-CPE	512	16	1024	768	4
SigLIP2	ViT-B/16-512	512	16	1024	768	4
TIPS	ViT-B/14-HR	504	14	1296	768	4

The models differ in their native input resolutions: 224×224 for CLIP ViT-B/16 [18], DINO ViT-B/16 [3], DINOv3 ViT-B/16 [27] and C-RADIOv2 ViT-B/16-CPE [8, 19]; 512×512 for DINOv2 ViT-B/14 [16]; 504×504 for SigLIP2 B/16-512 [29]; and 448×448 for TIPS ViT-B/14-HR [13].

D Computational resources

All experiments were executed on the Snellius HPC cluster to ensure high-performance processing and reproducibility. We ran our experiments on a single A100 node consisting of $4 \times$ NVIDIA A100 GPUs and 72 CPU cores, with a maximum wall time of 30 hours allocated per job to account for memory and processing constraints.

Regarding software and environment settings, the search index was distributed using FAISS sharding across all available GPUs. We utilized a batch size of 4 for all runs. To ensure experimental consistency, a global random seed of 42 was set across Python, NumPy, PyTorch, and CUDA.

E Reproduction results

Table 8: **Reproduction results.** We report accuracy (%) at different evaluation scales. “Reported” indicates values taken from prior published results, while “Reproduced” refers to our reproduction with a batch size (BS). Bold values highlight the best result for each model-scale configuration. Overall, our reproduced scores are close to or exceed the reported results in the original paper.

Model	Source	1024×10^2	1024×10^3	1024×10^4
ViT-S/16	Reproduced, BS: 256	37.5	45.0	–
	Reproduced, BS: 64	37.9	45.1	49.3
	Reported, BS: 64	37.2	43.1	46.6
ViT-B/16	Reproduced, BS: 64	48.0	54.7	–
	Reproduced, BS: 32	47.8	54.6	–
	Reproduced, BS: 8	–	–	57.9
	Reported, BS: 64	44.9	50.8	55.7
ViT-S/14	Reproduced, BS: 64	69.6	75.1	77.0
	Reported, BS: 64	70.2	74.9	77.0
ViT-B/14	Reproduced, BS: 64	68.0	74.0	–
	Reproduced, BS: 8	–	–	76.6
	Reported, BS: 64	69.1	74.6	76.9
ViT-L/14	Reproduced, BS: 64	64.1	71.2	–
	Reproduced, BS: 8	–	–	74.4
	Reported, BS: 64	64.6	71.7	74.8
ViT-G/14	Reproduced, BS: 32	62.4	–	–
	Reproduced, BS: 16	–	70.1	–
	Reproduced, BS: 8	–	–	73.3
	Reported, BS: 64	62.3	69.9	73.6

F Additional results

F.1 Experiment A

In experiment A, we assess model generalization across view-angle difficulties using per-class performance curves. In the figures below, the bars represent mean mIoU for unseen validation bins, and dots mark reference viewpoints. Performance typically declines as viewpoint distance increases from the reference bins, consistent with the trend in Figure 2. Across viewpoint difficulties, DINOv3, DINOv2, DINO, and CLIP consistently outperform all other models. C-RADIOv2 follows closely, while SigLIP2 and especially TIPS degrade substantially under extreme viewpoints (with TIPS showing the weakest overall robustness). DINOv3 generally outperforms all models; however, this does not hold for the *coat rack* and *guitar stand* classes, where, in the Extreme difficulty scenario, it becomes one of the worst-performing models.

Across all models, the background class performs best; other classes that perform well are *durian*, *broccoli*, and *strings*. These tend to generalize above average under unseen viewpoints. In contrast, *bed*, *coat rack*, *guitar stand*, and *sink* perform worst (the largest negative generalization gaps). For the *sink* class, DINOv3 significantly outperforms all other models. For *bed*, the drop is explained by poor ground-truth annotations that likely reduce model scores (as explored in Appendix F.1.1).

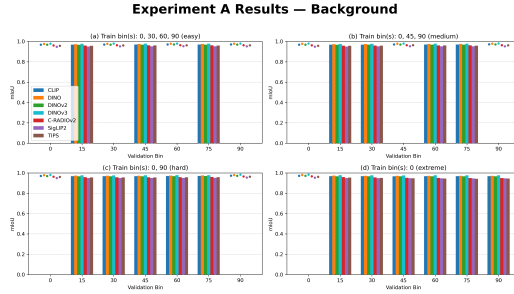


Figure 5: **Experiment A: background.** Viewpoint generalization for the background class across 4 training difficulty settings: (a) easy, (b) medium, (c) hard, and (d) extreme. All models achieve near-perfect consistency across bins, indicating that the background segmentation task remains invariant to viewpoint changes.

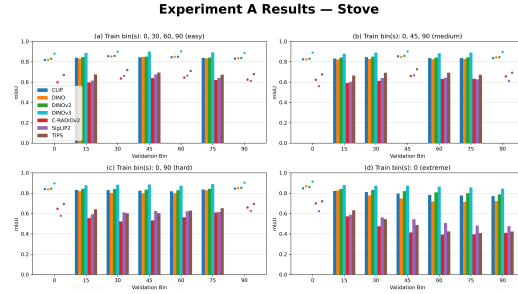


Figure 6: **Experiment A: stove.** The stove class perform slightly above the dataset average shown in Figure 2. The mIoU remains consistently high, and relative difference stays positive across all models. SigLIP2 and CLIP show the strongest viewpoint robustness. Degradation across validation bins follows the general pattern of Figure 2, with no major model-specific failures.

Experiment A Results — Bed

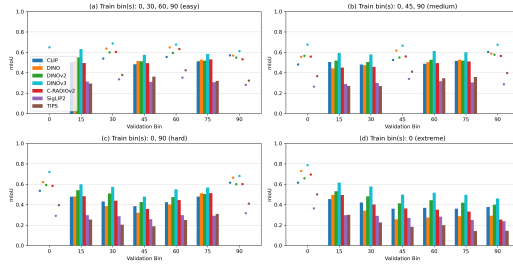


Figure 7: **Experiment A: bed.** The bed class scores far below the all-class baseline, with its mIoU scores remaining low even for strong models. This degradation is largely explained by systematically incorrect ground-truth masks, as seen in Figures 21–26 we analyze in Appendix F.1.1. The figure reflects this annotation-driven performance drop.

Experiment A Results — Toy cat

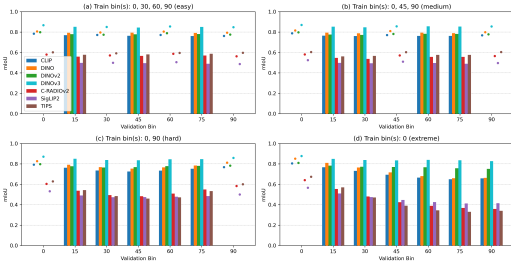


Figure 8: **Experiment A: toy cat.** The toy cat performance is very similar to the dataset-wide average observed in Figure 2, with relative differences near zero. Strong models (CLIP, DINO v1-v3) achieve high mIoU (0.77–0.84), and accuracy drops consistently across difficulty settings.

Experiment A Results — Sofa

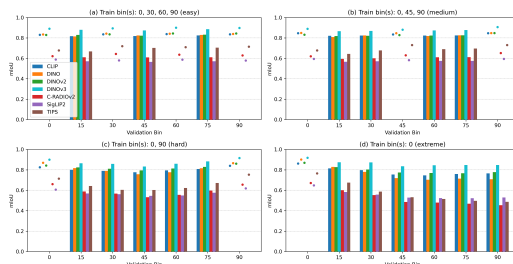


Figure 9: **Experiment A: sofa.** The sofa class performs slightly above the overall class average for every model and difficulty setting. The mIoU performance decreases smoothly with increased viewpoint difficulty, matching the overall experiment A trend observed in Figure 2.

Experiment A Results — Microwave

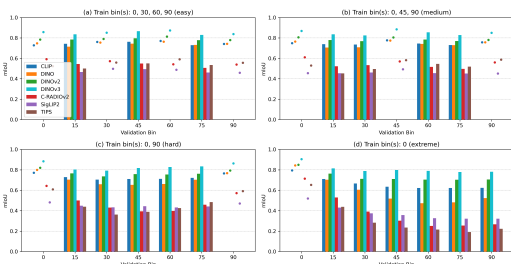


Figure 10: **Experiment A: microwave.** This class underperforms relative to Figure 2, with the largest drops appearing under Hard and Extreme difficulty. Model behavior diverges notably: DINOv3, DINOv2 and CLIP maintain comparatively strong performance, whereas DINO shows a mild decline. TIPS and SigLIP2 appear to struggle when segmenting the microwave category and degrade sharply under the Extreme condition, with a pronounced collapse beyond the 45° bin. Despite these weaker generalization patterns, the overall degradation across viewpoint bins follows the expected trend.

Experiment A Results — Toy cow

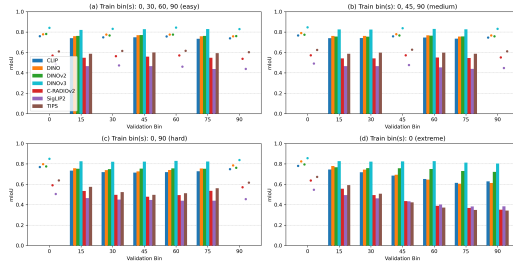


Figure 11: Experiment A: toy cow. The toy cow category shows slightly lower performance across all models on unseen bins, placing it among the weaker classes. Most noticeable is the lower performance of SIGLIP2 in the easy and medium task (see for example angle bin 75° in the easy task).

Experiment A Results — Toy dragon

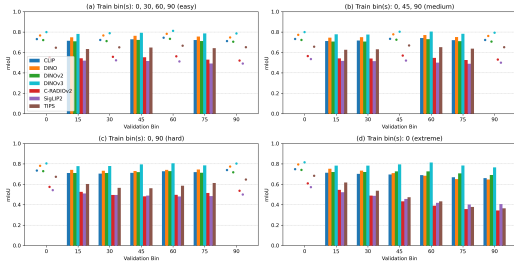


Figure 12: Experiment A: toy dragon. This class exhibits mildly negative gaps, in particular C-RADIOv2 is always lower than TIPS (when comparing to Figure 2). As a whole though, its performance trends mirror the general degradation observed of weaker models struggling as viewpoint distance increases.

Experiment A Results — Coat rack

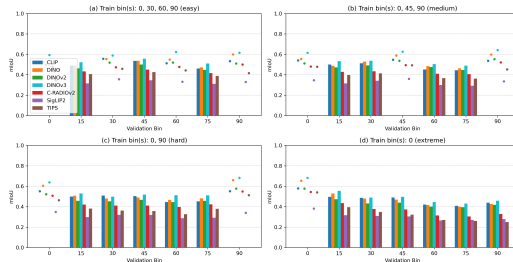


Figure 13: Experiment A: coat rack. The coat rack is the worst-performing class overall, with mIoU remaining below 0.7 across all validation bins. As seen in Figure 4, the object’s structure is extremely thin, which likely makes it highly sensitive to viewpoint changes and contributes to its weak generalization. It remains an open question whether this difficulty is intrinsic to the geometry or arises from dataset-specific factors. This could be an area of further investigation.

Experiment A Results — Guitar stand

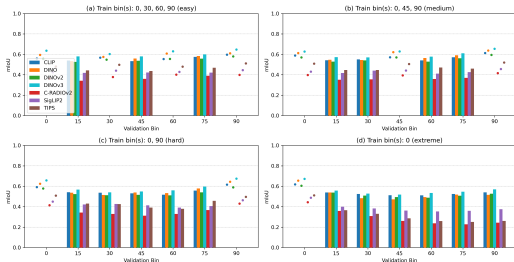


Figure 14: Experiment A: guitar stand. The Guitar stand class scores well below the baseline for all models and difficulties. Like the coat rack, the thin structure likely contributes to poor performance. However, the exact cause remains unclear and is a point for future investigation .

Experiment A Results — Ceiling lamp

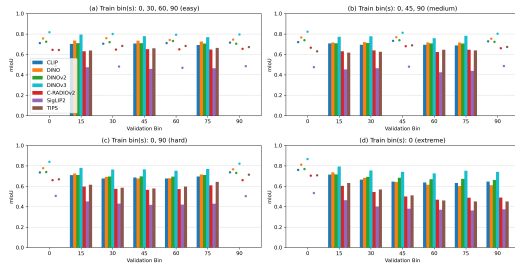


Figure 15: Experiment A: ceiling lamp. Performance trends closely mirror the general degradation observed in Figure 2, indicating the class has average viewpoint robustness. Degradation across bins follows the expected trend, with no unusual model failures.

Experiment A Results — Toilet

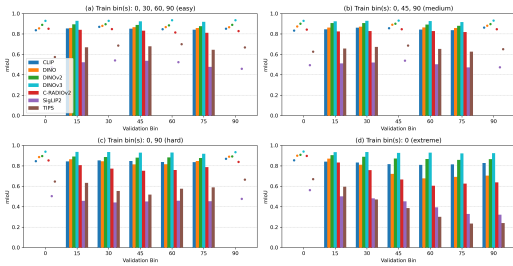


Figure 16: Experiment A: toilet. The toilet class consistently performs above the overall trend in Figure 2, with C-RADIOv2 showing the strongest boost, achieving increases of nearly 0.2 mIoU across difficulty levels.

Experiment A Results — Sink

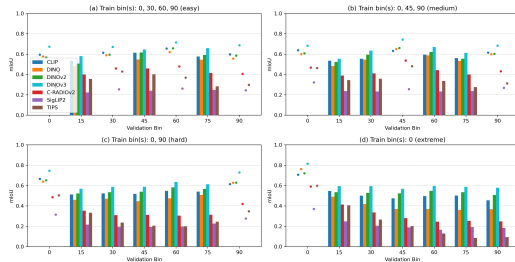
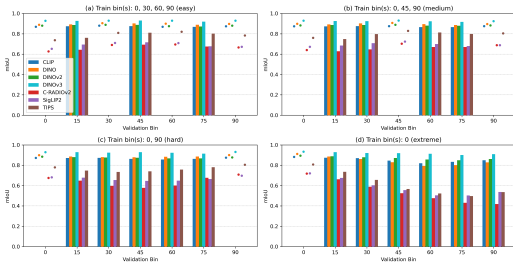


Figure 17: Experiment A: sink. The sink class is one of the three worst-performing classes in the dataset. DINOv3 is the only model that performs well in this category. All other models show large negative gaps relative to Figure 2, with SigLIP2 already underperforming in the easy setting by roughly 0.2 mIoU. Absolute scores generally remain low across all difficulty levels, and the degradation with viewpoint variation is steep. What geometric or appearance factors make sinks perform poorly is not immediately obvious, suggesting that sink segmentation is a broader failure mode worth investigating.

Experiment A Results — Strings



Experiment A Results — Broccoli

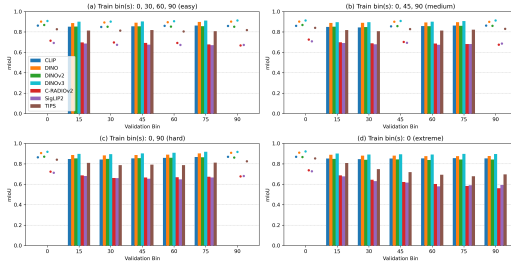


Figure 19: Experiment A: broccoli. Models generalize well on the broccoli class, maintaining stable and above-average performance across unseen viewpoint bins. DINOv3 is consistently the top performer, the other DINO-based models and CLIP following closely. TIPS also performs strongly, trailing just behind the leaders in all but the Extreme setting and achieving notably higher scores than in Figure 2. The results invite further investigation into which aspects of broccoli’s geometry support such robust viewpoint generalization.

Experiment A Results — Durian

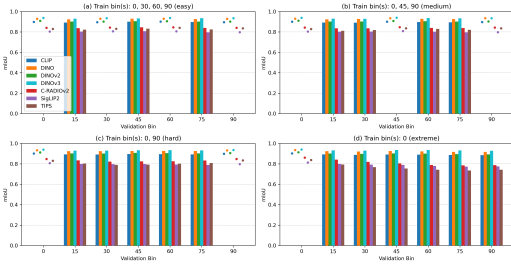


Figure 20: Experiment A: durian. Durian is among the best-performing classes, showing high absolute mIoU (0.78–0.94) across most models and all difficulty levels. This robustness is somewhat surprising: although the durian has a rich surface texture, its overall geometry is nearly spherical. It remains unclear whether the stable segmentation under viewpoint shifts stems from its distinctive visual signature or from contextual cues in the surrounding scene, such as the curtains highlighted in Figure 4.

F.1.1 Bed category ground truth analysis

We investigated the poor performance of the *bed* class (as seen in Figure 7) and identified inconsistent or incomplete ground truth annotations as a likely cause.



Figure 21: **Bed image example 1.** Original image used for annotation.

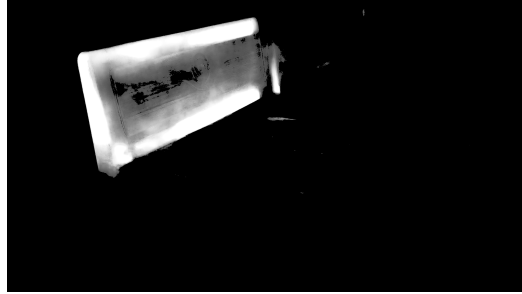


Figure 22: **Incomplete annotation.** Ground truth excludes parts of the bed (side railing, footboard) and ignores surrounding beds.



Figure 23: **Bed image example 2.** Original image used for annotation.

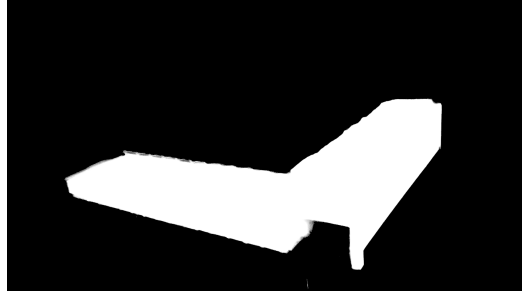


Figure 24: **Erroneous annotation.** The ground truth excludes large parts of the bed (headboard, mattress) and incorrectly includes the shadow between two beds.



Figure 25: **Bed image example 3.** Original image used for annotation.

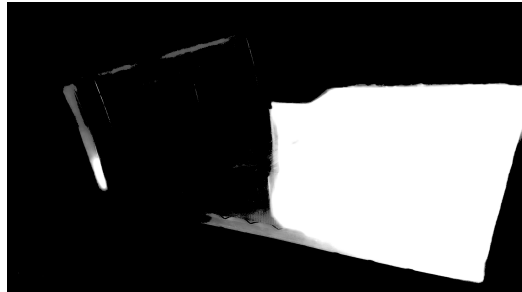


Figure 26: **Annotation error.** The ground truth omits the surrounding beds, incorrectly includes the gap between the main bed and the bed to its right, and only partially marks the headboard (side only).

F.2 Experiment B

As shown in Figure 3 and Figure 27, most models exhibit a gradual performance decline as the distance of the validation bin from the training bin (0°) increases. Visually, only C-RADIOv2 (ViT-B/16-CPE) and TIPS (ViT-B/14-HR) exhibit sharp performance drops with increasing validation angles, indicating limited generalization capacity under extreme viewpoint shifts.

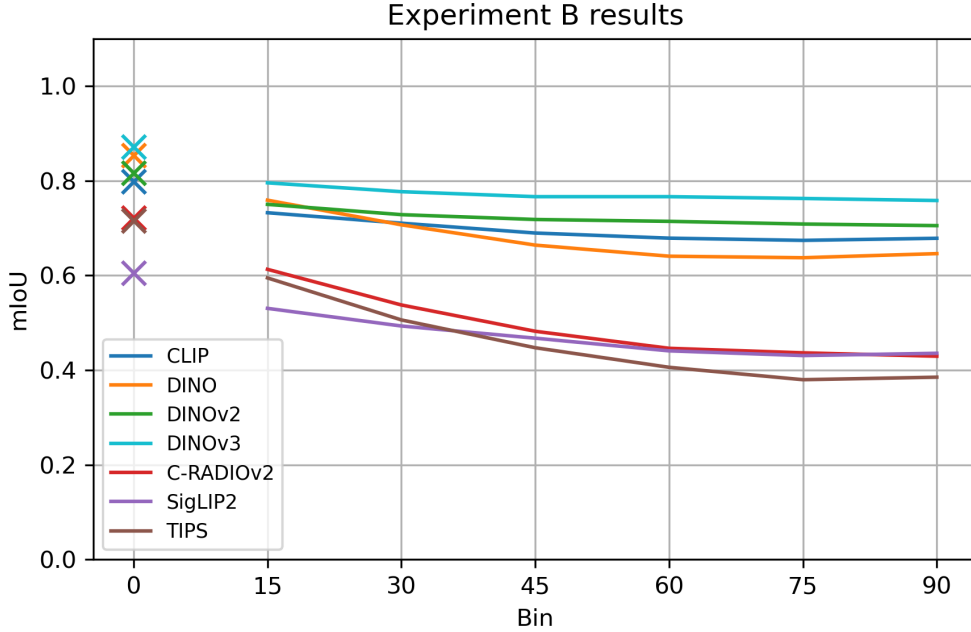


Figure 27: **Absolute mIoU under viewpoint shifts.** Each curve shows the mIoU of a model evaluated on increasing validation bins, measured directly (without normalization to the 0° baseline). The horizontal axis represents viewpoint angle relative to the training bin (0°), and the vertical axis shows the segmentation performance via mIoU. All models show a gradual decrease as the angular distance grows, reflecting reduced correspondence between memory and query views. DINOv2 has the most consistent generalization across bins, maintaining a high mIoU across all bins. DINOv3 maintains the highest mIoU. By contrast, TIPS displays the steepest decline (dropping by more than 0.2 between 15 and 75), confirming its reduced robustness under large viewpoint changes.

F.3 Experiment C

In Experiment C, we evaluate the impact of memory bank size on model performance. Table 9 reports the absolute mIoU gains per difficulty level when increasing the memory bank size (a) from 320k to 640k, (b) from 640k to 1,024k, and (c) from 320k to 1,024k. This highlights how the sensitivity to additional memory varies across model architectures, while also showing diminishing returns as memory size increases.

To put these performance gains into practical context, we summarize the computational setup of Experiment C. As mentioned in Appendix D, all experiments were executed on a single NVIDIA A100 GPU node with 4 GPUs. Across all configurations, runs took approximately 7–11 hours to complete, with larger memory banks consistently leading to longer runtimes. At larger memory sizes, runs encountered out-of-memory (OOM) errors unless additional measures were applied. We therefore fixed the batch size to 4 and enabled FAISS index sharding, reflecting the higher computational demands of larger memory configurations.

Table 9: **Performance gains from memory.** We report absolute mIoU improvements when increasing memory from (a) 320k to 640k, (b) 640k to 1,024k, and (c) 320k to 1,024k. Values are computed as differences from Table 4, with the final column showing the average gain across all 4 difficulty levels.

Model	Gains				
	Easy	Medium	Hard	Extreme	Average
(a) Memory: 320k → 640k					
CLIP ViT-B/16	0.017	0.016	0.017	0.013	0.016
DINO ViT-B/16	0.027	0.025	0.024	0.019	0.024
DINOv2 ViT-B/14	0.017	0.014	0.015	0.012	0.014
DINOv3 ViT-B/16	0.011	0.010	0.007	0.003	0.008
C-RADIOv2 ViT-B/16-CPE	0.041	0.036	0.033	0.024	0.034
SigLIP2 B/16-512	0.035	0.030	0.029	0.023	0.029
TIPS ViT-B/14-HR	0.044	0.038	0.032	0.016	0.033
Average per task	0.027	0.024	0.022	0.016	0.022
(b) Memory: 640k → 1,024k					
CLIP ViT-B/16	0.010	0.008	0.007	0.007	0.008
DINO ViT-B/16	0.014	0.013	0.012	0.010	0.012
DINOv2 ViT-B/14	0.009	0.008	0.008	0.007	0.008
DINOv3 ViT-B/16	0.006	0.005	0.003	0.002	0.004
C-RADIOv2 ViT-B/16-CPE	0.024	0.021	0.019	0.015	0.020
SigLIP2 B/16-512	0.023	0.020	0.019	0.015	0.019
TIPS ViT-B/14-HR	0.023	0.019	0.017	0.009	0.017
Average per task	0.015	0.014	0.012	0.009	0.013
(c) Memory: 320k → 1,024k					
CLIP ViT-B/16	0.026	0.024	0.024	0.020	0.024
DINO ViT-B/16	0.041	0.038	0.036	0.030	0.036
DINOv2 ViT-B/14	0.025	0.022	0.023	0.019	0.022
DINOv3 ViT-B/16	0.016	0.015	0.010	0.005	0.012
C-RADIOv2 ViT-B/16-CPE	0.065	0.058	0.053	0.039	0.054
SigLIP2 B/16-512	0.058	0.050	0.047	0.038	0.048
TIPS ViT-B/14-HR	0.067	0.057	0.049	0.025	0.049
Average per task	0.043	0.038	0.035	0.025	0.035

G Qualitative analysis

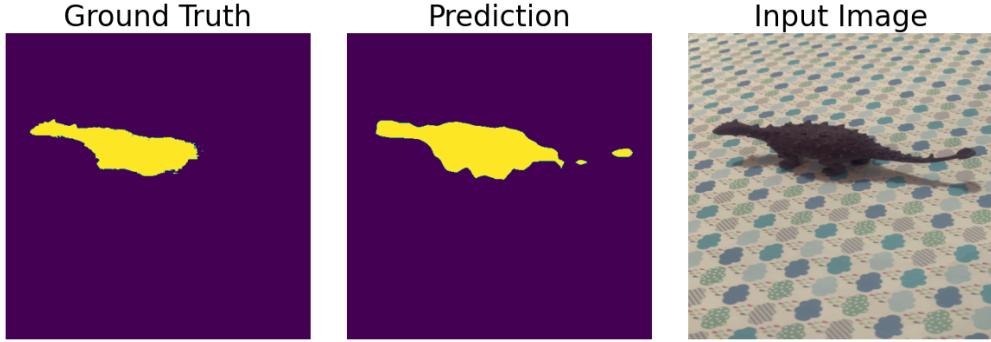


Figure 28: **Qualitative segmentation.** Results shown using DINO. Left: input image. Center: predicted mask. Right: ground truth mask. Interestingly, the prediction of the *toy dragon* aligns more closely with visible object boundaries than the ground truth, which appears coarser and less accurate at fine details (e.g., tail, horns, stomach occlusion).



Figure 29: **Overlay comparison of ground truth and prediction.** The same instance as in Figure 28 is shown for a better comparison. Left: ground truth overlaid on the input image. Center: prediction overlaid on the input image. Right: difference visualization, with the ground truth overlaid on the predicted mask.

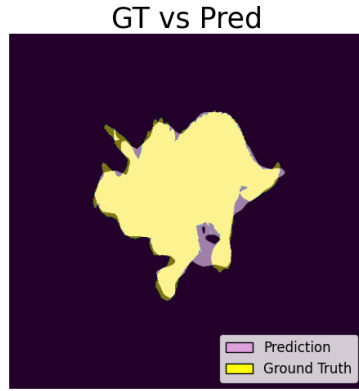


Figure 30: **Another overlay comparison of ground truth and prediction.** Shown using DINO. Yellow: ground truth mask. Purple: predicted mask. We note that discrepancies appear at fine-grained boundaries (e.g., tail, horns, nose) and in occluded or shadowed regions (e.g., under the stomach).